RSC Advances

PAPER

View Article Online
View Journal | View Issue

Cite this: *RSC Adv.*, 2025, **15**, 27139

Feature-rich fundamental properties of hydrogen-adsorbed armchair graphene nanoribbons: insights from first-principles calculations†

D. M. Hoat,[ab] Khuong Dien Vo,[c] Ngoc Thanh Thuy Tran,[d] Quoc Duy Ho,[e] Minh Triet Dang,[f] Huynh Anh Huy,[f] Duong Trong Nhan *[gh] and Duy Khanh Nguyen[gh]

Using first-principles calculations, we report on the notable structural, electronic, and magnetic properties of hydrogen-adsorbed 7-armchair graphene nanoribbons (7-AGNR) at various adatom concentrations and distributions. Key findings include optimal structural parameters, adsorption energies, one-dimensional electronic band structures, density of states (DOS), charge density distributions, charge density differences, and spin density distributions. Our results indicate that hydrogen atoms preferentially adsorb on the top sites of carbon atoms, with double-side adsorption being more stable than single-side adsorption. Even-hydrogenated 7-AGNR configurations behave as nonmagnetic semiconductors with varying bandgaps, while odd-hydrogenated configurations exhibit ferromagnetic behavior with different bandgaps. The number of unpaired hydrogen adatoms influences the magnetic moments of these configurations. Specifically, the magnetic moment can reach up to 7 μ_B for complete single-side hydrogenation, while all other odd-hydrogenated configurations generally display a magnetic moment of 1 μ_B. This behavior is attributed to the complex hybridization between hydrogen and carbon orbitals. This research highlights the potential of hydrogen-adsorbed 7-AGNR systems for applications in advanced electronics, optoelectronics, and spintronics.

Received 18th June 2025
Accepted 24th July 2025

DOI: 10.1039/d5ra04327a

rsc.li/rsc-advances

1 Introduction

Since the first isolation of two-dimensional (2D) graphene, many graphene-like 2D materials have been subject to intensive investigation, driven by their exceptional properties and potential applications across numerous technological fields.[1–7] As the dimensionality of these 2D materials is further reduced to one-dimensional (1D) structures, such as nanoribbons or nanotubes, the quantum confinement effect becomes increasingly enhanced. This quantum confinement leads to unique electronic and optical properties not observed in bulk or 2D materials, making 1D materials promising candidates for many applications.[8–14] Graphene nanoribbons (GNRs), with their unique electronic, mechanical, and optical properties, hold immense potential for revolutionizing various technological fields. Their narrow width and edge structure give rise to quantized electronic states and tunable bandgaps,[15,16] making them ideal candidates for applications in nanoelectronics, such as field-effect transistors (FETs), quantum computing, and energy conversion.[17,18] Additionally, their high charge carrier mobility, strong spin–orbit coupling, and sensitivity to external perturbations make GNRs attractive for next-generation electronics, spintronic devices, and biosensors.[19] GNRs have been successfully synthesized through both top-down and bottom-up approaches. Top-down techniques, like photolithography and unzipping carbon nanotubes (CNTs), yield GNRs with well-defined geometries.[20,21] Conversely, bottom-up methods, such as chemical vapor deposition (CVD), offer greater control over material properties, including edge structure and doping levels, making them more suitable for electronic applications.[22,23]

The successful synthesis of GNRs makes it easier to study the properties and application of these materials. Among the published studies, the magnetic property of 7-atom wide armchair graphene nanoribbons (7-AGNR) has garnered significant interest due to their potential applications in spintronics and

[a]*Institute of Theoretical and Applied Research, Duy Tan University, Ha Noi 100000, Vietnam*
[b]*Faculty of Natural Sciences, Duy Tan University, Da Nang 550000, Vietnam*
[c]*FPT University, Can Tho Campus, Can Tho, Vietnam*
[d]*Hierarchical Green-Energy Materials (Hi-GEM) Research Center, National Cheng Kung University, Tainan 701, Taiwan*
[e]*Department of Mathematics and Physics, Universitetet i Stavanger, Stavanger, Norway*
[f]*Faculty of Physics, School of Education, Can Tho University, Can Tho City, Vietnam*
[g]*Laboratory for Computational Physics, Institute for Computational Science and Artificial Intelligence, Van Lang University, Ho Chi Minh City, Vietnam. E-mail: nhan.duongtrong@vlu.edu.vn*
[h]*Faculty of Mechanical – Electrical and Computer Engineering, School of Technology, Van Lang University, Ho Chi Minh City, Vietnam*

† Electronic supplementary information (ESI) available. See DOI: https://doi.org/10.1039/d5ra04327a

quantum computing. While the 7-AGNR are generally considered non-magnetic in their pristine state, recent studies have indicated that specific modifications can induce magnetic behavior. Pizzochero and Kaxiras demonstrated that introducing edge extensions can cause a magnetic ground state in non-magnetic 7-AGNR.[24] This aligns with theoretical predictions that localized states at the edges can give rise to magnetism in graphene structures.[25] Introducing defects or doping can also influence the magnetic properties of 7-AGNR. Dai *et al.* reported that defects, such as grain boundaries, can localize electronic states and lead to distinct magnetic behaviors compared to pristine AGNR.[26] Functionalization, particularly hydrogenation, has been shown to modify graphene nanoribbons' electronic and magnetic properties. The presence of hydrogen atoms at the edges can lead to the formation of edge radicals, which may contribute to localized magnetic moments.[27]

Hydrogenation can also affect the bandgap of the 7-AGNR, which is a significant area of research because hydrogenation can modify the electronic properties of these nanostructures, potentially enhancing their applicability in various electronic devices. The hydrogenation of graphene nanoribbons leads to a transition from sp^2 to sp^3 hybridization in the carbon atoms, which is associated with forming a band gap. According to the findings by Kharche *et al.*, hydrogenation can induce a bandgap in AGNR, which is not present in their pristine state.[28] Liu *et al.* reported that the band gap of hydrogenated 7-AGNR can be finely modulated by the density of functional groups attached to the nanoribbon.[29] Their study indicated that fully hydroxylated 7-AGNRs exhibit a band gap of approximately 0.7 eV, while the bandgap of partially hydrogenated structures can vary, demonstrating the sensitivity of the electronic properties to the degree of hydrogenation. Usually, the hydrogenation causes enlargement of the 7-AGNRs' bandgaps. The experiment conducted by Sung *et al.* shows that the bandgap of nanoribbons is reduced.[30] They assumed that the bandgap reduction originates from the interaction with the Au(111) substrate.

To date, a systematic computational study to determine the essential properties and underlying physical and chemical mechanisms of various hydrogen-adsorbed 7-AGNR is absent, an interesting topic with high potential applications. To comprehensively address this outlined issue, we carry out a thorough first-principles investigation to determine the structural, electronic, and magnetic characteristics of the hydrogen-adsorbed 7-AGNR under various concentrations and distributions, in which the optimal adsorption sites, single-side, and double-side adsorptions are fully included in the investigation to make general results. The density functional theory (DFT) quantities to determine the essential fundamental properties of the various hydrogen-adsorbed 7-AGNR systems are developed, including the optimal structural parameters, adsorption energies, 1D electronic band structures, density of states, spatial charge density distributions, charge density distributions, and spin density distributions. Under the developed DFT quantities, the underlying mechanisms to enrich the electronic and magnetic behaviors are elucidated, which can provide a deep understanding of various hydrogen-adsorbed graphene nanoribbons for potential applications.

2 Computational details

DFT calculation performed in the Vienna *ab initio* simulation package (VASP)[31,32] is a powerful tool in simulating the electronic structure of condensed matter systems, which has been applied from quantum computation to environmental studies.[33–37] In this work, the VASP calculations are performed to investigate the structural, electronic, and magnetic properties of the pristine and hydrogen-adsorbed 7-AGNR. One-dimensional (1D) 7-AGNR system is constructed by finite-size

Table 1 Adsorption concentration (%), energy adsorption (eV), minimum C–C bond length/1st C–C (Å), maximum C–C bond length/2nd C–C (Å), H–C bond length (Å), C–C–C angle (°), and planar/buckled structure

System	Configuration	Ratio of H adatom and C atom	Concentration (%)	$E_{adsorption}$ (eV)	1st C–C (Å)	2nd C–C (Å)	H–C (Å)	C–C–C angle (°)	Planar/ buckled
7-AGNR	Pristine	X	X	X	1.375	1.433	X	121.25	Planar
	$(1H)_{edge\text{-}C1}$	1H : 14C	7.14%	−2.4939	1.377	1.486	1.12	121.91	Buckled
	$(1H)_{non\text{-}edge\text{-}C5}$	1H : 14C	7.14%	−1.7289	1.366	1.498	1.13	122.42	Buckled
	$(2H)_{C1\text{–}C13\text{-}double}$	2H : 14C	14.28%	−3.5812	1.378	1.514	1.11	113.26	Buckled
	$(3H)_{C1\text{-}to\text{-}C3\text{-}double}$	3H : 14C	21.42%	−3.2353	1.373	1.531	1.11	108.30	Buckled
	$(4H)_{C1\text{-}to\text{-}C4\text{-}double}$	4H : 14C	28.57%	−3.6445	1.362	1.519	1.11	109.36	Buckled
	$(5H)_{C1\text{-}to\ C5\text{-}double}$	5H : 14C	35.71%	−3.4339	1.371	1.529	1.11	109.32	Buckled
	$(6H)_{C1\text{-}to\text{-}C6\text{-}double}$	6H : 14C	42.85%	−3.6762	1.359	1.514	1.11	109.76	Buckled
	$(7H)_{C1\text{-}to\text{-}C7\text{-}single}$	7H : 14C	50%	−1.9203	1.464	1.492	1.16	114.67	Buckled
	$(7H)_{C1\text{-}to\text{-}C7\text{-}double}$	7H : 14C	50%	−3.5165	1.379	1.521	1.12	109.93	Buckled
	$(8H)_{C1\text{-}to\text{-}C8\text{-}double}$	8H : 14C	57.14%	−3.6149	1.379	1.516	1.11	109.58	Buckled
	$(9H)_{C1\text{-}to\text{-}C9\text{-}double}$	9H : 14C	64.28%	−3.5072	1.382	1.545	1.12	110.69	Buckled
	$(10H)_{C1\text{-}to\text{-}C10\text{-}double}$	10H : 14C	71.42%	−3.6535	1.371	1.527	1.11	109.47	Buckled
	$(11H)_{C1\text{-}to\text{-}C11\text{-}double}$	11H : 14C	78.57%	−3.6238	1.377	1.557	1.11	109.84	Buckled
	$(12H)_{C1\text{-}to\text{-}C12\text{-}double}$	12H : 14C	85.71%	−3.7148	1.331	1.536	1.11	109.62	Buckled
	$(13H)_{C1\text{-}to\text{-}C13\text{-}double}$	13H : 14C	92.85%	−3.6114	1.458	1.532	1.12	109.89	Buckled
	$(14H)_{C1\text{-}to\text{-}C14\text{-}double}$	14H : 14C	100%	−3.4560	1.505	1.521	1.11	109.62	Buckled

edge cutting along the *y*-axis of the 2D graphene, with a 15 Å vacuum layer to ensure isolation between periodic images. Passivation of hydrogen atoms at the edges eliminates the dangling bonds. The Perdew–Burke–Ernzerhof (PBE) functional[38] within the generalized gradient approximation (GGA) are used to describe the exchange–correlation interactions. Meanwhile, projector-augmented wave (PAW) pseudopotentials[39] are used to model the ion–electron interactions. In addition, Heyd–Scuseria–Ernzerhof (HSE06) functional[33,34] are utilized to enhance accuracy in calculating bandgaps of the semiconducting systems. As reported in Table 2, the HSE06 bandgaps for the pristine 7-AGNR, $(1H)_{edge\text{-}C1}$, and $(1H)_{non\text{-}edge\text{-}C5}$ configurations are enhanced about 0.26 eV to 0.56 eV as compared with their PBE ones. A plane-wave energy cutoff of 500 eV is adopted. Structural optimizations are performed using a $12 \times 1 \times 1$ *k*-point mesh. Subsequent self-consistent calculations employed a higher $100 \times 1 \times 1$ *k*-point mesh. Convergence criteria of 10^{-7} eV for total energy and 10^{-2} eV Å^{-1} for forces are applied in the calculation process. The 1D electronic band structure is calculated along the one-dimensional Brillouin zone using the Monkhorst–Pack method,[40] leveraging self-consistent results. This approach provides a comprehensive understanding of the electronic properties of the systems under investigation.

3 Results and discussions

The 7-AGNR system is created by cutting the graphene sheet along its armchair edges and four hydrogen atoms (purple balls) are added to the edge carbon atoms (brown balls) to saturate the dangling bonds and stabilize the structure. Fig. 1(a) shows that the 7-AGNR consists of 7 dimer lines. Carbon atoms labeled C1 to C14 represent potential adsorption sites for hydrogen atoms. The edge-saturated hydrogen atoms labeled H1 to H4 are bonded to carbon atoms at the edges of the nanoribbon. For investigation of hydrogen adsorption, the most optimal adsorption position of the hydrogen atom (adatom) is found at the top site (adatom stabilizing on the top of carbon atom) among other bridge and hollow sites, regardless of any adatom concentrations. Notedly, different kinds of adsorption atoms could result in different optimal adsorption sites on the graphene nanoribbons.[41–43] The optimal adsorption adatoms are labeled from H5 to H14 as increasing adsorption adatom numbers. As a result, two typical adsorption sites can represent all other sites: *e.g.*, H adatom on the edge carbon atoms (C1, C2, C13, C14) and H adatom on other non-edge carbon atoms. The two typical optimal adsorption sites for the single adatom are termed $H_{edge\text{-}C1}$ and $H_{non\text{-}edge\text{-}C5}$ configurations. Besides, with the increased number of H adatoms, the single-side and double-side adsorptions are considered. The single-side adsorption means all H adatoms are situated in the same plane, while the double-side adsorption means that H adatoms are located in both opposite planes. Notably, the adsorption concentration (concentration) is defined by the ratio of H adatoms per C atoms. Following these definitions, the single H adsorption on the edge carbons of 7-AGNR is denoted as $(1H)_{edge\text{-}C1}$ and presented in Fig. 1(b). Notably, this hydrogen adsorption induced local structural buckling, as evident from

Table 2 Band gap (eV), magnetic moment (μ_B), and magnetism of the pristine and hydrogen-adsorbed 7-AGNR configurations

System	Configuration	Ratio of H adatom and C atom	Concentration (%)	PBE/HSE06 bandgap (eV)	Magnetic moment (μ_B)	Nonmagnetism (NM)/ ferromagnetism (FM)
7-AGNR	Pristine	X	X	PBE/HSE06: 1.62/1.93	0	NM
	$(1H)_{edge\text{-}C1}$	1H : 14C	7.14%	PBE/HSE06 (up): 0.9/1.16 PBE/HSE06 (dn): 1.08/1.67	1.0	FM
	$(1H)_{non\text{-}edge\text{-}C5}$	1H : 14C	7.14%	PBE/HSE06 (up): 0.94/1.34 PBE/HSE06 (dn): 1.24/1.80	1.0	FM
	$(2H)_{C1\text{–}C13\text{-}double}$	2H : 14C	14.28%	PBE: 0.99	0	NM
	$(3H)_{C1\text{-}to\text{-}C3\text{-}double}$	3H : 14C	21.42%	PBE (up): 1.06 PBE (dn): 1.12	1.0	FM
	$(4H)_{C1\text{-}to\text{-}C4\text{-}double}$	4H : 14C	28.57%	PBE: 0.41	0	NM
	$(5H)_{C1\text{-}to\text{-}C5\text{-}double}$	5H : 14C	35.71%	PBE (up): 1.42 PBE (dn): 1.52	1.0	FM
	$(6H)_{C1\text{-}to\text{-}C6\text{-}double}$	6H : 14C	42.85%	PBE: 2.42	0	NM
	$(7H)_{C1\text{-}to\text{-}C7\text{-}single}$	7H : 14C	50%	PBE (up): 3.09 PBE (dn): 2.94	7.0	FM
	$(7H)_{C1\text{-}to\text{-}C7\text{-}double}$	7H : 14C	50%	PBE (up): 1.37 PBE (dn): 1.62	1.0	FM
	$(8H)_{C1\text{-}to\text{-}C8\text{-}double}$	8H : 14C	57.14%	PBE: 1.60	0	NM
	$(9H)_{C1\text{-}to\text{-}C9\text{-}double}$	9H : 14C	64.28%	PBE (up): 1.76 PBE (dn): 2.04	1.0	FM
	$(10H)_{C1\text{-}to\text{-}C10\text{-}double}$	10H : 14C	71.42%	PBE: 0.83	0	NM
	$(11H)_{C1\text{-}to\text{-}C11\text{-}double}$	11H : 14C	78.57%	PBE (up): 2.72 PBE (dn): 2.85	1.0	FM
	$(12H)_{C1\text{-}to\text{-}C12\text{-}double}$	12H : 14C	85.71%	PBE: 4.36	0	NM
	$(13H)_{C1\text{-}to\text{-}C13\text{-}double}$	13H : 14C	92.85%	PBE (up): 3.18 PBE (dn): 3.06	1.0	FM
	$(14H)_{C1\text{-}to\text{-}C14\text{-}double}$	14H : 14C	100%	PBE: 4.24	0	NM

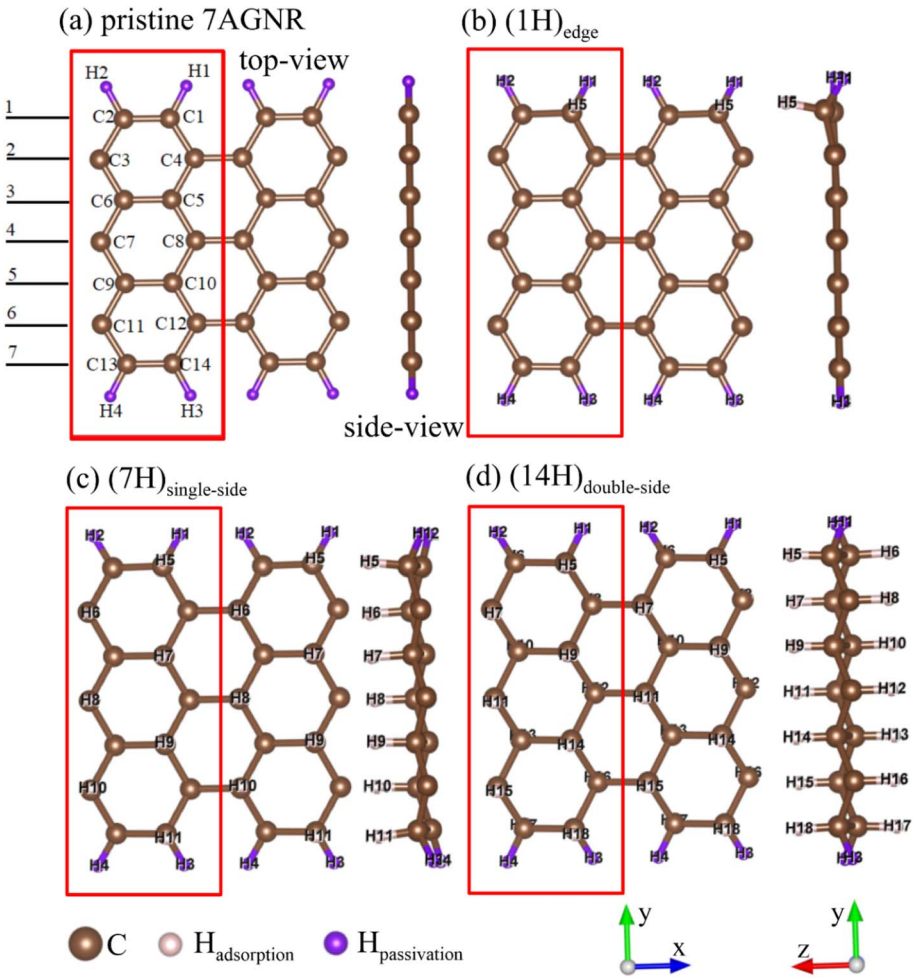

Fig. 1 Optimal geometric structures of (a) pristine 7AGNR, (b) $(1H)_{edge\text{-}C1}$, (c) $(7H)_{C1\text{-}to\text{-}C7\text{-}single}$, and (d) $(14H)_{C1\text{-}to\text{-}C14\text{-}double}$ configurations. The solid black number along the *y* direction (dimer line) and red rectangle display the width of the system and its unit, respectively. The C positions in the unit cell from C1 to C14 illustrate the possible adsorption positions of H atoms.

the side view of the $(1H)_{edge\text{-}C1}$. This suggests that the further increase of adatoms leads to higher buckling. The single-side adsorption with the possible maximum number of H adatoms on the 7-AGNR is only the seven hydrogen adatoms, which can adsorb on the seven specific carbon atoms of C1, C3, C5, C7, C9, C11, and C13. This highest single-sided H adsorption is denoted by the $(7H)_{C1\text{-}to\text{-}C7\text{-}single}$ configuration, as shown in Fig. 1(c). In contrast, the maximum number of 100% $H_{double\text{-}side}$ adsorption is doubly higher than that of the single-side one, whereas each H adatom covers each carbon atom in both opposite planes. This maximum double-side H adsorption can be denoted as $(14H)_{C1\text{-}to\text{-}C14\text{-}double}$ configuration, which is depicted in Fig. 1(d). Furthermore, the 7-AGNR optimally adsorbed with other H concentrations are created using the aforementioned rule: *e.g.*, $(2H)_{C1\text{–}C13\text{-}double}$, $(3H)_{C1\text{-}to\text{-}C3\text{-}double}$, $(4H)_{C1\text{-}to\text{-}C4\text{-}double}$, $(5H)_{C1\text{-}to\text{-}C5\text{-}double}$, $(6H)_{C1\text{-}to\text{-}C6\text{-}double}$, $(7H)_{C1\text{-}to\text{-}C7\text{-}double}$, $(8H)_{C1\text{-}to\text{-}C8\text{-}double}$, $(9H)_{C1\text{-}to\text{-}C9\text{-}double}$, $(10H)_{C1\text{-}to\text{-}C10\text{-}double}$, $(11H)_{C1\text{-}to\text{-}C11\text{-}double}$, $(12H)_{C1\text{-}to\text{-}C12\text{-}double}$, and $(13H)_{C1\text{-}to\text{-}C13\text{-}double}$ configurations presented in Tables 1 and 2, in which the 2H or 13H, subscript C1–C13 or C1-to-C13, and subscript double illustrate for the number of adsorbed H adatoms, the H adsorbed on specific C sites at C1 and C13 (C1–C13) or at C1–C2–C3–C4–C5–C6–C7–C8–C9–C10–C11–C12–C13 (C1-to-C13), and double-side adsorptions, respectively. For clear figure out of the specific H adsoprtion sites, we have included the all posible adsorption sites of the typical 2H adsorbed on 7-AGNR in the supporting Fig. S1.†

The initially created pristine and hydrogen-adsorbed 7-AGNR systems configurations are rigorously optimized to achieve the most optimal configurations. As a result, the optimal structural parameters of the most optimal configurations, including the C–C bond lengths at the edge and non-edge carbon atoms (1st and 2nd C–C), H–C bond lengths, C–C–C bond angles, and buckling features, are presented in Table 1. Besides, the adsorption energies (E_{ad}), which can reveal the stability of these nanoribbons, are reported in Table 1. For the 7-AGNR system with n number of hydrogen atoms adsorbed, the E_{ad} can be calculated as the average difference between the ground-state energies of the hydrogenated system (E_{total}), the pristine 7-AGNR system ($E_{pristine}$), and n isolated carbon atoms (E_{carbon}), which the formula for the E_{ad} is established as $E_{ad} = (E_{total} - E_{pristine} - E_{carbon})/n$. As reported in Table 1, the E_{ad} of all

configurations is negative, indicating that the formation of hydrogenated 7-AGNR systems is energetically favorable. All these configurations are stable, with E_{ad} ranging from −3.71 eV to −1.73 eV. The values of E_{ad}, as reported in Table 1, reveal a rule that the adsorption of an even number of hydrogen atoms results in a more stable structure than the odd number of hydrogen atoms, which signifies that the H–H bonding is more stable than the H–C bonding. Specifically, for the lowest H adsorption concentration, the $(1H)_{edge\text{-}C1}$ configuration is much more stable than the $(1H)_{non\text{-}edge\text{-}C5}$ configuration: *e.g.*, E_{ad} = −2.4939 eV for $(1H)_{edge\text{-}C1}$ configuration and E_{ad} = −1.7289 eV for the $(1H)_{non\text{-}edge\text{-}C5}$ configuration. As the number of hydrogen atoms exceeds (12H), the adsorption energy (E_{ad}) slightly decreases. This result can be explained through orbital hybridization, where the H-1s orbitals interact with the C-2p_z orbitals, denoted as s-p_z hybridization, for further discussion. As the concentration of hydrogen increases, the $(13H)_{C1\text{-}to\text{-}C13\text{-}double}$ and $(14H)_{C1\text{-}to\text{-}C14\text{-}double}$ configurations may cause some minor rearrangement of orbital orientation, making the structure less stable owing to its higher E_{ad}. Significantly, when seven H atoms are added to one side of the pristine 7-AGNR called the $(7H)_{C1\text{-}to\text{-}C7\text{-}single}$ configuration, the orbital distribution symmetry is notably disrupted, making it much less stable (E_{ad} = −1.92 eV) compared to its double-side $(7H)_{C1\text{-}to\text{-}C7\text{-}double}$ configuration (E_{ad} = −3.52 eV). The much higher stability of the double-side structure than the single-side structure remains valid for all adatom concentrations. This implies that the double-side configurations should be preferably considered for experimental synthesis.

Moreover, modification in optimal structural parameters of the adsorbed configurations is identified by comparing the structural difference of the adsorbed configurations with the pristine configuration, as reported in Table 1. For the pristine 7-AGNR configuration, the 1st C–C (bond between edge C atoms) and 2nd C–C (bond between non-edge C atoms) are 1.375 Å and 1.43 Å, respectively. The different C–C bond lengths throughout the pristine 1D system are owing to its finite-size edge termination. The non-identical bond lengths are the typical feature of the 1D nanoribbons compared with the uniform bond lengths of its 2D derivative. In the $(1H)_{edge\text{-}C1}$ and $(1H)_{non\text{-}edge\text{-}C5}$ configurations, the 1st C–C bond lengths remain the same because the 1st C–C bond lengths in pristine 7-AGNR are preferably affected by the edge H passivation. On the other hand, the 2nd C–C bond lengths increase by 0.06–0.07 Å because the orbital interaction weakens these bonds. Furthermore, an increase in the number of H adatoms adsorbed leads to an increase in the 2nd C–C bond lengths in all high H configurations, except for the $(7H)_{C1\text{-}to\text{-}C7\text{-}single}$ configuration. At 92.85% adsorption $(13H)_{C1\text{-}to\text{-}C13\text{-}double}$ and 100% adsorption $(14H)_{C1\text{-}to\text{-}C14\text{-}double}$, the 1st C–C bond lengths become shorter and longer, respectively. Because the s-p_z is out-of-plane orbitals, it mainly causes structural buckling with a slight effect on the symmetry of the hydrogenated 7-AGNRs. As reported in Table 1, the C–C–C angle in the pristine 7-AGNR is 121.25°, which nearly remains the same in the $(1H)_{edge\text{-}C1}$ and $(1H)_{non\text{-}edge\text{-}C5}$ structures. At higher hydrogen concentrations, this angle slightly changes to 108.30°–114.67°. This result signifies that the H-1s orbitals also interact with C-2p_{xy} orbitals.

Halogens and transition metal adatoms are well-known to induce ferromagnetism in graphene and silicene by modifying their structures.[44–46] To gain deeper insights into the structural modifications and their impact on electronic properties, we calculated the bandgap, magnetic moment, and magnetism of pristine and hydrogenated 7-AGNR configurations reported in Table 2. Interestingly, the 7-AGNR absorbed with an even number of hydrogen atoms, the $(2H)_{C1\text{–}C13\text{-}double}$, $(4H)_{C1\text{-}to\text{-}C4\text{-}double}$, $(6H)_{C1\text{-}to\text{-}C6\text{-}double}$, $(8H)_{C1\text{-}to\text{-}C8\text{-}double}$, $(10H)_{C1\text{-}to\text{-}C10\text{-}double}$, $(12H)_{C1\text{-}to\text{-}C12\text{-}double}$, and $(14H)_{C1\text{-}to\text{-}C14\text{-}double}$ configurations exhibit non-magnetic semiconducting behavior. In contrast, those with an odd number of hydrogen atoms, the $(1H)_{edge\text{-}C1}$, $(1H)_{non\text{-}edge\text{-}C5}$, $(3H)_{C1\text{-}to\text{-}C3\text{-}double}$, $(5H)_{C1\text{-}to\text{-}C5\text{-}double}$, $(7H)_{C1\text{-}to\text{-}C7\text{-}double}$, $(9H)_{C1\text{-}to\text{-}C9\text{-}double}$, $(11H)_{C1\text{-}to\text{-}C11\text{-}double}$, and $(13H)_{C1\text{-}to\text{-}C13\text{-}double}$ configurations, are ferromagnetic semiconductors with consistent magnetic moment of 1 μ_B. Critically, the $(7H)_{C1\text{-}to\text{-}C7\text{-}single}$ configuration displays the maximum magnetic moment of 7 μ_B. However, the magnetic stability of the $(7H)_{C1\text{-}to\text{-}C7\text{-}single}$ configuration is significantly smaller than its double-side $(7H)_{C1\text{-}to\text{-}C7\text{-}double}$ configuration. Due to these unique characteristics, the 1D electronic band structures of the even-hydrogenated 7-AGNR configurations are presented without spin-splitting bands (Fig. 2). In contrast, the spin-splitting 1D electronic band structures are accompanied by the odd-hydrogenated 7-AGNR configurations (Fig. 3).

Fig. 2(a) depicts the non-spin-splitting 1D band structure of the pristine 7-AGNR, with the contribution analysis of the C-2s, C-2p_{xy}, and C-p_z orbitals highlighted in cyan, blue, and red, respectively. Unlike 2D graphene, a zero-gap material, the quantum confinement in the 1D structure of the 7-AGNR introduces a bandgap of 1.62/1.93 eV (PBE/HSE06), as reported in Table 2. This bandgap separates the conduction band minimum (CBM) and valence band maximum (VBM), both located at the G-point of the Brillouin zone, making the pristine 7-AGNR with a direct bandgap. The C-2p_z orbitals play a crucial role in the electronic structure of the pristine 7-AGNR, significantly contributing to low-lying energies to create the π bands. In contrast, the C-2p_{xy} orbitals primarily contribute at energy levels below −3 eV, while the C-2s orbitals begin to emerge around −5.5 eV. The C-2p_{xy} and C-2s related bands belong to the σ bands. At deeper energy levels in the valence bands, the C-2p_z orbitals interact with the C-2p_{xy} and C-2s orbitals. Since the C-2p_z orbitals correspond to π orbitals and the C-2s and C-2p_{xy} orbitals correspond to σ orbitals, their hybridization reflects an overlap between sp^2 and sp^3 orbitals. This observation will be further investigated through its latter density of states analysis.

Previous DFT studies have suggested that hydrogenation of 7-AGNRs reduces aromaticity while increasing aliphatic character, typically resulting in a larger bandgap.[47] However, experimental measurements by Sung *et al.* revealed an unexpected decrease in the bandgap of hydrogenated 7-AGNRs. Without explicit electronic structure calculations, they attributed this bandgap reduction to interactions between the 7-AGNRs and the Au (111) substrate.[48] Firstly, the nanoribbons' bandgap variation is shown to originate from the complex

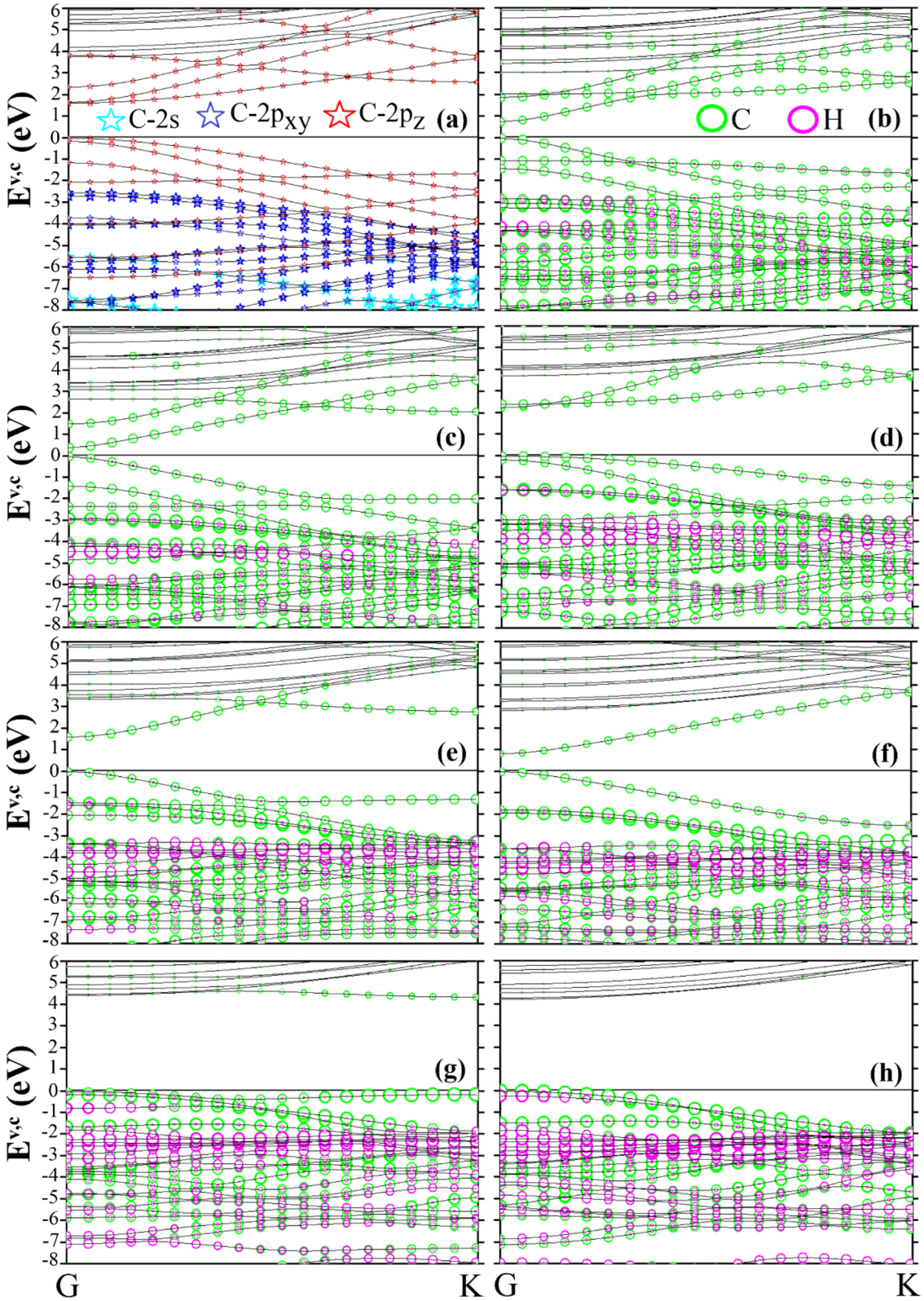

Fig. 2 Orbital- and atom-decomposed electronic band structures of (a) pristine 7AGNR, (b) $(2H)_{C1-C13\text{-}double}$, (c) $(4H)_{C1\text{-}to\text{-}C4\text{-}double}$, (d) $(6H)_{C1\text{-}to\text{-}C6\text{-}double}$, (e) $(8H)_{C1\text{-}to\text{-}C8\text{-}double}$, (f) $(10H)_{C1\text{-}to\text{-}C10\text{-}double}$, (g) $(12H)_{C1\text{-}to\text{-}C12\text{-}double}$, and (h) $(14H)_{C1\text{-}to\text{-}C14\text{-}double}$ configurations. The cyan, blue, and red stars show for the C-2s, C-2p_{xy}, and C-2p_z orbitals, respectively, and the green and magenta circles expose the C and H atoms.

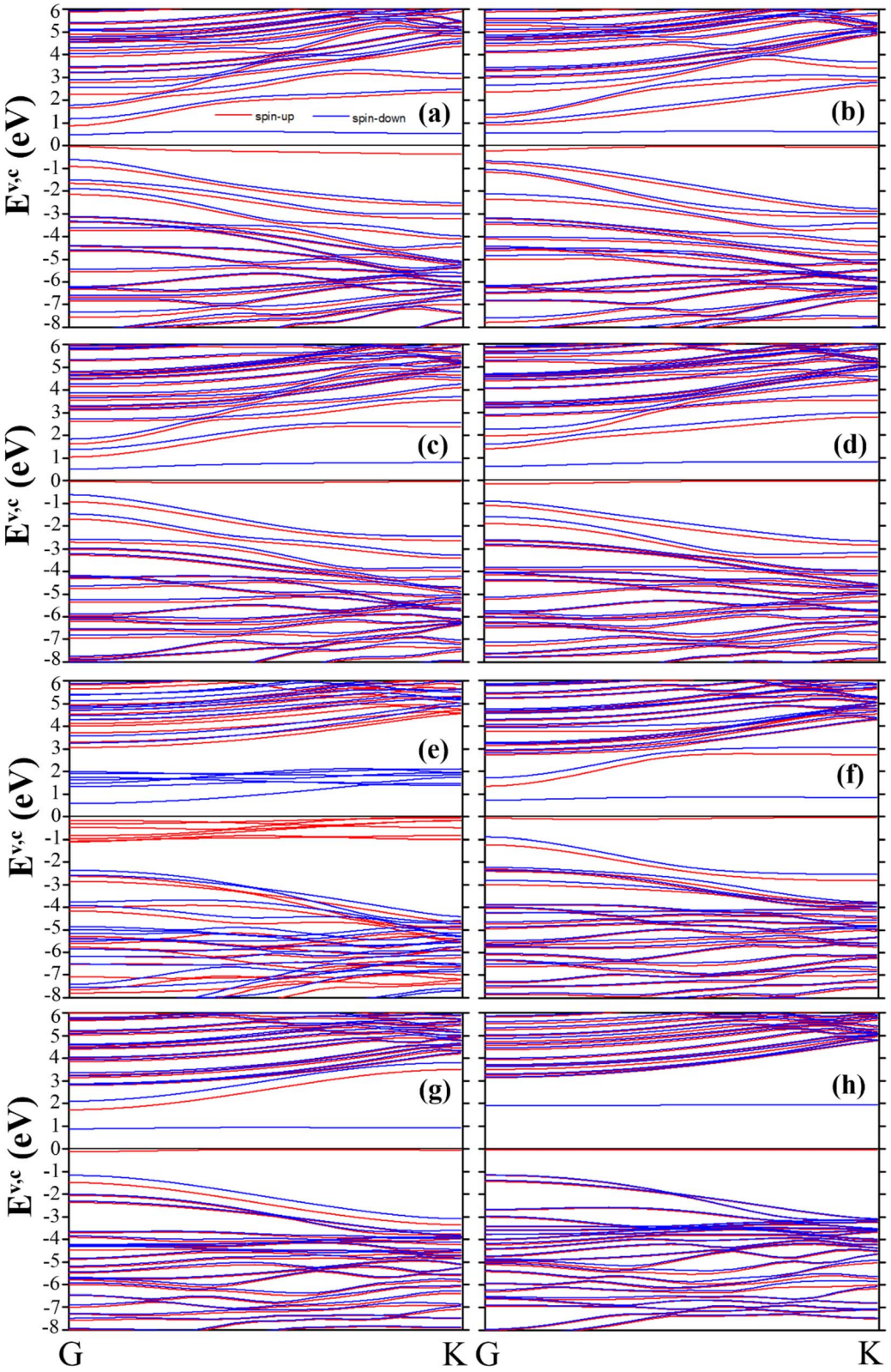

Fig. 3 Spin-splitting energy bands of (a) $(1H)_{edge\text{-}C1}$, (b) $(1H)_{non\text{-}edge\text{-}C5}$, (c) $(3H)_{C1\text{-}to\text{-}C3\text{-}double}$, (d) $(5H)_{C1\text{-}to\text{-}C5\text{-}double}$, (e) $(7H)_{C1\text{-}to\text{-}C7\text{-}single}$, (f) $(7H)_{C1\text{-}to\text{-}C7\text{-}double}$, (g) $(9H)_{C1\text{-}to\text{-}C9\text{-}double}$, and (h) $(13H)_{C1\text{-}to\text{-}C13\text{-}double}$ configurations. The solid red and blue lines display the spin-up and spin-down bands, respectively.

orbital hybridization, where π orbitals play an essential role.[49] Secondly, the distribution and concentration of adatoms are also crucial factors affecting the electronic properties of the nanoribbons.[50] Therefore, our comprehensive electronic structure calculations of various hydrogen-adsorbed 7-AGNR systems can clarify the underlying mechanism of the bandgap reduction. Our calculated bandgaps of hydrogen-adsorbed 7-AGNR configurations are reported in Table 2, whereas both bandgap reduction/enlargement are observed below/beyond the critical concentration, respectively. Except for some exclusive cases, the bandgap initially decreases with low H concentrations (up to 57%) but significantly increases at higher H concentrations. This behavior can be attributed to the distribution of hydrogen adatoms on the 7-AGNR, which can alter the C–C bond lengths and C–C–C angles and orbital hybridization between hydrogen and carbon atoms. To gain deeper insights into these effects, the atom-decomposed 1D electronic band structures of the $(2H)_{C1–C13\text{-double}}$, $(4H)_{C1\text{-to-}C4\text{-double}}$, $(6H)_{C1\text{-to-}C6\text{-double}}$, $(8H)_{C1\text{-to-}C8\text{-double}}$, $(10H)_{C1\text{-to-}C10\text{-double}}$, $(12H)_{C1\text{-to-}C12\text{-double}}$, and $(14H)_{C1\text{-to-}C14\text{-double}}$ configurations are analyzed, as depicted in Fig. 2(b) to (h), respectively. The size of the magenta and green circles illustrates the contribution intensities of the H adatoms and C atoms.

In Fig. 2(b), (c), (e) and (f), the s-bands of H adatoms are predominantly located in the deeper valence energy bands (magenta circles). In contrast, they are co-dominated by the bands of C atoms (green circles). The co-domination of the bands of H adatoms and C atoms at more profound valence energies implies the hybridization of H-1s and C-($2p_z$ and $2p_{xy}$) orbitals. This disrupts the extended π-electron network and leads to the formation of localized electronic states. Consequently, the π-electrons lose their delocalization across the hydrogenated 7-AGNRs, reducing band gaps. As summarized in Table 2, the bandgaps of the $(2H)_{C1–C13\text{-double}}$, $(4H)_{C1\text{-to-}C4\text{-double}}$, $(8H)_{C1\text{-to-}C8\text{-double}}$, and $(10H)_{C1\text{-to-}C10\text{-double}}$ configurations decrease to 0.99 eV, 0.41 eV, 1.6 eV, and 0.83 eV, respectively. These effects are sensitive to the spatial distribution of hydrogen atoms. In contrast, for the $(6H)_{C1\text{-to-}C6\text{-double}}$ configuration, shown in Fig. 2(d), the co-domination of H adatoms and C atoms appears at upper energy levels within the valence bands. This implies that the H-1s orbitals hybridize with the C-$2p_z$ orbitals at upper valence energies. This hybridization enhances the delocalization of π-electrons, significantly increasing the bandgap to 2.42 eV. At higher hydrogen concentrations, such as 85.71% and 100%, a high contribution density of the bands of H adatoms occurs in wider valence energy bands, where the H-1s orbitals strongly hybridize with the C-$2p_z$ orbitals. As a result, the bandgaps of the $(12H)_{C1\text{-to-}C12\text{-double}}$ and $(14H)_{C1\text{-to-}C14\text{-double}}$ configurations increase dramatically to 4.36 eV and 4.24 eV, respectively, shown in Fig. 2(g) and (h). The mechanism for changing the bandgap caused by different H concentrations is identified as follows: the H-1s orbitals can either enhance or inhibit the delocalization of π-electrons *via* hybridization with π orbitals of C, leading to a corresponding increase or decrease in the bandgap. Specifically, at sufficiently high H concentrations (from 78.57% to 100%), the sufficiently high density of H-1s orbitals becomes prominent at the upper valence bands, significantly widening the bandgap (Table 2). Below the critical concentration of 78.57%, the bandgaps are decreased or increased, strongly dependening on the specific concentrations and distributions (Table 2). The mechanism for bandgap modification of the 2D systems under different external factors has been observed in previous studies.[51–53]

The spin-splitting 1D energy bands for the hydrogen-adsorbed 7-AGNR configurations with odd H numbers of $(1H)_{edge\text{-}C1}$, $(1H)_{non\text{-}edge\text{-}C5}$, $(3H)_{C1\text{-to-}C3\text{-double}}$, $(5H)_{C1\text{-to-}C5\text{-double}}$, $(7H)_{C1\text{-to-}C7\text{-single}}$, $(7H)_{C1\text{-to-}C7\text{-double}}$, $(9H)_{C1\text{-to-}C9\text{-double}}$ and $(13H)_{C1\text{-to-}C13\text{-double}}$ are presented in Fig. 3(a) and (h), respectively. The spin-up bands are depicted with red lines, while blue lines illustrate spin-down bands. Except for the $(7H)_{C1\text{-to-}C7\text{-single}}$ configuration, all other odd-hydrogenated 7-AGNRs exhibit similar electronic features, including a distinct spin-splitting in the vicinity of the Fermi level, resulting in a uniform magnetic moment of 1 μ_B. In these structures, the VBM is composed of spin-up bands, while the CBM is composed of spin-down bands. As a result, these odd-hydrogenated 7-AGNR configurations are ferromagnetic semiconductors with the spin-splitting bandgaps reported in Table 2. As for the $(7H)_{C1\text{-to-}C7\text{-single}}$ configuration with all seven H adatoms adsorbed on the same side, it possesses a higher spin-splitting 1D electronic band structure as depicted in Fig. 3(e), in which there are more spin-up (red lines) and spin-down (blue lines) bands appearing in the upper valence and lower conduction bands, respectively. The energy levels deeper than −2.4 eV in the valence band and those higher than 2 eV in the conduction band are filled with slightly separate blue and red lines, signifying the spin-splitting in these energy levels. Closer to the Fermi level, the upper valence energy bands from −1 eV to below the Fermi level are exclusively composed of spin-up bands, and the higher conduction energy bands from 0.5 to 2 eV are formed solely by spin-down bands. This substantial spin-splitting feature results in the most considerable magnetic moment of 7 μ_B for the $(7H)_{single\text{-}edge}$ configuration, which is also an unusual ferromagnetic semiconductor. As shown in Table 2, the spin-up/spin-down 1D bandgaps for odd double-side configurations of $(1H)_{edge\text{-}C1}$, $(1H)_{non\text{-}edge\text{-}C5}$, $(3H)_{C1\text{-to-}C3\text{-double}}$, $(5H)_{C1\text{-to-}C5\text{-double}}$, $(7H)_{C1\text{-to-}C7\text{-double}}$, $(9H)_{C1\text{-to-}C9\text{-double}}$ and $(13H)_{C1\text{-to-}C13\text{-double}}$ are 0.9/1.08 eV, 0.94/1.24 eV, 1.06/1.12 eV, 1.42/1.52 eV, 1.37/1.62 eV, 1.76/2.04 eV, 2.72/2.85 eV, 3.18/3.06 eV, respectively. Unlike the double-side (7H) configuration, the spin-up/spin-down bandgaps of the $(7H)_{C1\text{-to-}C7\text{-single}}$ configuration show different values of 3.09/2.94 eV. Unlike even-hydrogenated 7-AGNRs, the spin-splitting 1D bandgaps of odd-hydrogenated 7-AGNRs consistently increase with hydrogen concentrations. This suggests that hydrogen pairs may weaken the interaction between H-1s and C-$2p_z$ orbitals at deeper energy levels in the valence band. The later discussion considers the density of states (DOS) of these configurations to further elucidate this behavior.

Fig. 4(a) presents the total DOS and orbital-decomposed DOSs of the pristine 7-AGNR, whereas the Fermi level is set at 0 eV, as remarked by the dashed line. The black curve represents the total DOS, while the contributions from the C-2s, C-$2p_{xy}$, and C-$2p_z$ orbitals are shown in cyan, blue, and magenta curves,

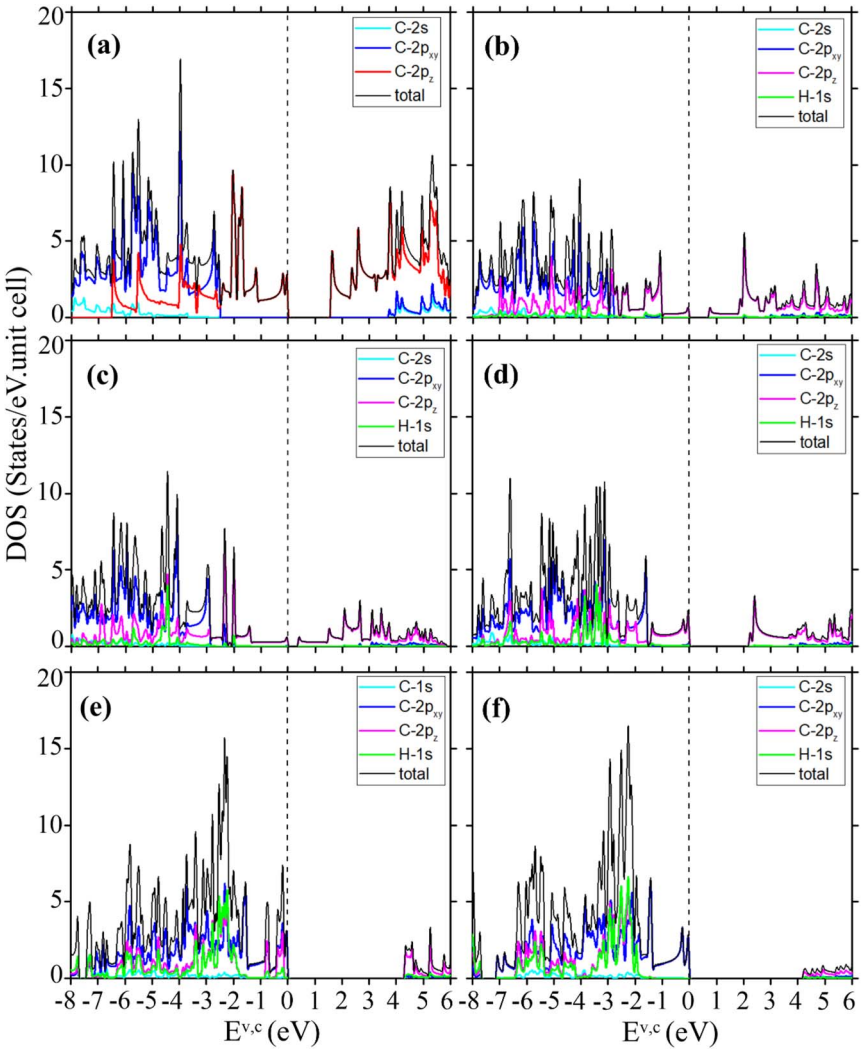

Fig. 4 Orbital-decomposed density of states (DOSs) (a) pristine 7AGNR, (b) $(2H)_{C1-C13\text{-double}}$, (c) $(4H)_{C1\text{-to-}C4\text{-double}}$, (d) $(6H)_{C1\text{-to-}C6\text{-double}}$, (e) $(12H)_{C1\text{-to-}C12\text{-double}}$, and (f) $(14H)_{C1\text{-to-}C14\text{-double}}$ configurations. The solid cyan, blue, magenta, and green curves display the C-2s, C-2p_{xy}, C-2p_z, and H-1s orbitals, respectively.

respectively. In Fig. 4(a), the total DOS reveals a bandgap of 1.62 eV, separating the valence and conduction bands. This corresponds to the direct bandgap observed in the electronic 1D band structure of Fig. 2(a), where both the VBM and CBM are located at the G-point of the Brillouin zone. Furthermore, the C-2p_z orbitals contribute to the π-states, while the C-2s and C-2p_{xy} orbitals form the σ-states. The upper valence energy bands, ranging from −2.5 eV below the Fermi level, primarily comprise π-states. Below −2.5 eV, the deeper valence energy bands are strongly dominated by σ-states that are hybridized with π-states in the range of −7.5 to −2.5 eV. The hybridization of C-2p_{xy} and C-2s orbitals forms the sp^2 hybridization, which maintains the planar structure of the pristine 7-AGNR. Meanwhile, the hybridization between π and σ orbitals weakens the π-bonds. The lowest conduction bands are mainly dominated by π-states. At higher energy levels (>3.5 eV), the weak sp^3 hybridization occurs, involving C-2p_{xy}, C-2p_z, and C-2s orbitals.

As for even-hydrogenated 7-AGNR configurations, their total- and orbital-decomposed DOSs are shown in Fig. 4(b)–(f). The contributions from the C-2s, C-2p_{xy}, C-2p_z, and H-1s orbitals are represented in cyan, blue, pink, and green, respectively. As illustrated in Fig. 4(b) for the DOSs of the $(2H)_{C1-C13\text{-double}}$ configuration, the adsorption of two hydrogen atoms induces the formation of sp^3 orbitals at energy levels below −3 eV, where hybridization between the H-1s, C-2p_{xy}, and C-2p_z orbitals occurs. This sp^3 hybridization causes a buckling of the (2H) structure, as detailed in Table 2. Simultaneously, the intensity of the C-2p_z orbitals near the Fermi level decreases significantly, disrupting the delocalized π-electron network and resulting in a reduced bandgap. The DOSs intensity of the conduction bands also diminishes markedly, with the C-2p_z orbitals remaining the dominant contribution at these energy levels. For the DOSs of the $(4H)_{C1\text{-to-}C4\text{-double}}$ configuration, shown in Fig. 4(c), the adsorption of higher hydrogen atoms amplifies these effects. The hybridized orbital intensities below −3 eV increase substantially, reducing the intensity of the C-2p_z orbitals near the Fermi level. This leads to a dramatic drop in the bandgap to 0.41 eV. With more hydrogen atoms adsorbed,

the structural symmetry of the nanoribbon changes, redistributing the H-1s orbitals. In the $(6H)_{C1\text{-}to\text{-}C6\text{-}double}$, $(12H)_{C1\text{-}to\text{-}C12\text{-}double}$, and $(14H)_{C1\text{-}to\text{-}C14\text{-}double}$ configurations, shown in Fig. 4(d)–(f), the H-1s orbitals interact with the C-2p_{xy} and C-2p_z orbitals at deeper energy levels in the valence bands. This interaction significantly increases the density of C-2p_z orbitals near the Fermi level, resulting in a notable enlargement of the bandgap. Additionally, the DOSs intensity of the lowest conduction bands of these high-even H configurations decreases significantly, reflecting further modifications in their electronic band structures.

In terms of verifying the spin-splitting 1D band structures of the odd-hydrogenated 7-AGNR configurations and clarifying the mechanism inducing these magnetic properties, their orbital- and spin-projected DOSs are considered *via* Fig. 5. The solid cyan, blue, magenta, and green curves represent the contributions of the C-2s, C-2p_{xy}, C-2p_z, and H-1s orbitals, respectively. The positive DOS values correspond to spin-up states, while negative DOS values correspond to spin-down states. As for the DOSs of the $(1H)_{edge\text{-}C1}$ configuration shown in Fig. 5(a), the low-lying valence energy bands near the Fermi level are primarily composed of the C-2p_z orbitals and a minor part of H-1s orbitals, the hybridization of which is responsible for π-bonding. The energy level of −3 eV can be considered a critical point; below this point, the contributions of C-2p_{xy} and C-2s are recognizable. These deeper valence bands are characterized by the hybridization of C-2p_z, H-1s, and C-2p_{xy} orbitals to form sp^3-hybridized bonds, leading to the observed buckling in the $(1H)_{edge\text{-}C1}$ configuration. The conduction bands are predominantly composed of C-2p_z orbitals. In the valence bands, while the C-2p_{xy} orbitals exhibit symmetric spin-up and spin-down states through the horizontal line, the H-1s and C-2p_z orbitals show significant spin polarization. This spin polarization is most pronounced near the Fermi level, where both H-1s and C-2p_z orbitals contribute. This spin polarization ultimately gives rise to a magnetic moment of 1 μ_B, classifying the $(1H)_{edge\text{-}C1}$

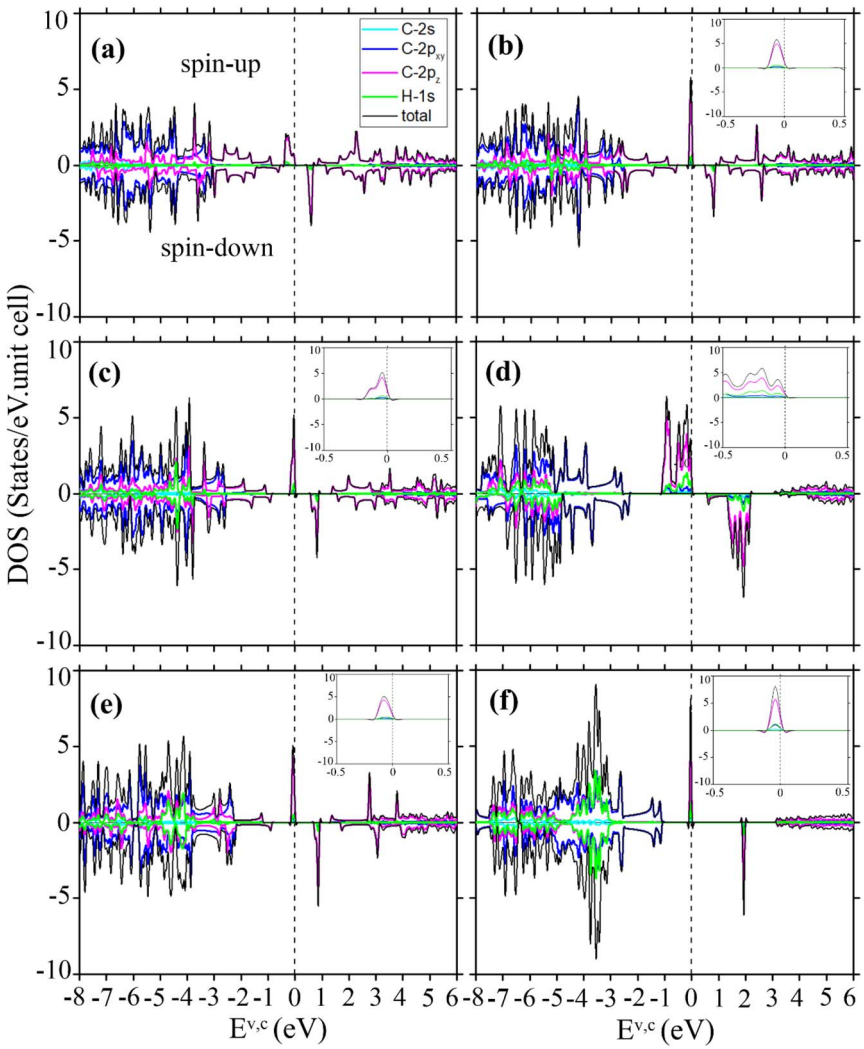

Fig. 5 Orbital- and spin-decomposed density of states (DOSs) (a) $(1H)_{edge\text{-}C1}$, (b) $(3H)_{C1\text{-}to\text{-}C3\text{-}double}$, (c) $(5H)_{C1\text{-}to\text{-}C5\text{-}double}$, (d) $(7H)_{C1\text{-}to\text{-}C7\text{-}single}$, (e) $(7H)_{C1\text{-}to\text{-}C7\text{-}double}$, and (f) $(13H)_{C1\text{-}to\text{-}C13\text{-}double}$ configurations. The solid cyan, blue, magenta, and green curves display for the C-2s, C-2p_{xy}, C-2p_z, and H-1s orbitals, respectively, and the positive and negative DOSs display for the spin-up and spin-down states.

configuration as a ferromagnetic semiconductor. For the positive DOS component, the bandgap between the highest spin-up valence band and the lowest spin-up conduction band is 0.94 eV (as reported in Table 2). This corresponds to the red curves' spin-up bandgap visualized in Fig. 3(a). Similarly, for the negative DOS, the bandgap gap between the spin-down valence band and the spin-down conduction band is 1.08 eV, as indicated in Table 2 and represented by the blue curves in Fig. 3(a).

As the number of hydrogen atoms adsorbed on the 7-AGNR increases, the spin polarization remains constant. Fig. 5(b), (c), (e) and (f) depict the DOSs of the $(3H)_{C1\text{-}to\text{-}C3\text{-}double}$, $(5H)_{C1\text{-}to\text{-}C5\text{-}double}$, $(7H)_{C1\text{-}to\text{-}C7\text{-}double}$, and $(13H)_{C1\text{-}to\text{-}C13\text{-}double}$ configurations, respectively. In these cases, the hybridization with additional H-1s orbitals significantly enhances the intensity of both spin-up and spin-down C-2p$_z$ orbitals. Notably, the C-2p$_z$ peaks near the Fermi level become sharper and more intense. Still, the difference in spin-up and spin-down densities remains constant, resulting in a unique magnetic moment of 1 μ_B for all four configurations. With the increase of the hydrogen atoms, the spin-up peaks at the Fermi level become thinner. To provide a clearer view of this region, a zoomed-in portion is displayed in the top right corner of each figure. Changes in the DOSs result in significant alterations to the bandgap. In the deeper valence bands, the hybridization between the H-1s, C-2p$_{xy}$, and C-2p$_z$ orbitals is substantially enhanced, strengthening the sp^3 character of the orbitals. This hybridization shifts the critical point to upper energy levels within the valence bands, amplifying its impact on the C-2p$_z$ orbitals near the Fermi level. As a result, the bandgap increases with the number of hydrogen atoms in the odd-hydrogenated 7-AGNRs, as summarized in Table 2.

Significantly, the adsorption of 7 hydrogen atoms on only one side of the 7-AGNR, the $(7H)_{C1\text{-}to\text{-}C7\text{-}single}$ configuration, causes strong asymmetry in the DOS structure, which can be observed in Fig. 5(d). Only spin-up orbitals occupy the valence bands from −1.5 below 0 eV, while only spin-down orbitals occupy the conduction bands from 0.5 to 2 eV. The significant difference in density of spin-up and spin-down peaks causes a high magnetic moment of 7 μ_B, making it a strong ferromagnetic semiconductor. This is due to creation of seven unpaired electrons in the system, in which each unpaired electron contributes 1 μ_B, leading to its net magnetic moment equal to 7 μ_B.[54] The critical point is shifted to a more bottomless valence band at −5 eV; below this point, the sp^3 hybridizations of the H-1s, C-2p$_{xy}$, and C-2p$_z$ orbitals on positive and negative components of the DOS spectrum are still symmetric like other four configurations. The significant difference is that the sp^3 hybridizations are also observed in the strong spin polarization region near the Fermi level. Consequently, the bandgap of $(7H)_{C1\text{-}to\text{-}C7\text{-}single}$ is significantly widened to 3.09 eV (spin-up) and 2.94 eV (spin-down). These bandgaps are comparable to those of the $(13H)_{C1\text{-}to\text{-}C13\text{-}double}$ configuration, even though the number of the H adatom in the $(7H)_{C1\text{-}to\text{-}C7\text{-}double}$ configuration is about half of that in the $(13H)_{C1\text{-}to\text{-}C13\text{-}double}$ configuration.

As mentioned earlier, the adsorption of hydrogen atoms on 7-AGNR induces significant changes in its structural, electronic, and particularly magnetic properties. These effects are highly dependent on hydrogen atoms' concentration and spatial distribution. To better understand the mechanisms driving these changes, the charge density distribution and charge density difference for the pristine 7-AGNR, as well as the $(1H)_{edge\text{-}C1}$, $(7H)_{C1\text{-}to\text{-}C7\text{-}double}$, $(13H)_{C1\text{-}to\text{-}C13\text{-}double}$, and $(14H)_{C1\text{-}to\text{-}C14\text{-}double}$ configurations, are presented in Fig. 6. The charge density is measured in ea_0^{-3}, where e is the elementary charge and a_0 is the lattice constant. The maximum charge density is represented in red isosurface, while the minimum is shown in blue isosurface. For the charge density distribution of the pristine 7-AGNR configuration, as illustrated in Fig. 6(a), the region between two carbon atoms appears to be a dense red color, indicating the highest electron concentration in this area. This high electron density corresponds to the strong covalent σ bonding arising from the C-2s and C-2p$_{xy}$ orbitals, as shown in Fig. 4(a). Surrounding the C–C bond, the green regions indicate a lower electron concentration associated with forming π-bonds. This observation is consistent with the upper valence to low conduction bands in Fig. 4(a), which are predominantly occupied by the C-2p$_z$ orbitals. Under hydrogen adsorption effects, the charge density distributions are significantly modified, and the charge density differences are also formed. The modified charge density and charge density difference for the $(1H)_{edge}$ configuration are depicted in Fig. 6(b) and (c), respectively. Notably, the hydrogen adatom has a slightly lower electronegativity than the carbon atom, meaning the adsorbed H atom cannot significantly attract electrons from the carbon atom. However, Fig. 6(b) reveals a distinct electron distribution (red region) between the H and C atoms. This electron sharing arises from the interaction of the H-1s orbital with the C-2p$_{xy}$ and C-2p$_z$ orbitals, forming sp^3 hybridized orbitals. These hybridized orbitals create new energy states for electron occupancy, leading to the redistribution of electrons. This process, termed charge accretion, is visualized as yellow regions, while areas of electron depletion appear as blue regions. The sp^3 hybridization is depicted in Fig. 6(c): the upper yellow sphere represents the overlap of the H-1s and C-2p$_z$ orbitals, while the three remaining yellow lobes correspond to the interaction between H-1s and C-2p$_{xy}$ orbitals. This hybridization induces local buckling in the structure, as reported in Table 2. Additionally, weaker charge transfer occurs at the second and third neighboring carbon atoms, forming smaller yellow regions. Consequently, the extent of the red region between two C atoms, as shown in Fig. 6(b), is diminished. The green regions encompassing the C–C and H–C bonds signify the presence of elongated and weaker π-bonds, reflecting the structural and electronic alterations introduced by the H adsorption.

As the number of hydrogen atoms increases, the interaction between the H-1s, C-2p$_{xy}$, and C-2p$_z$ orbitals becomes increasingly pronounced. These orbital hybridizations concentrate more electron density around the hydrogen atoms, as evidenced by the larger red regions surrounding hydrogen atoms in the charge density plots for the $(7H)_{C1\text{-}to\text{-}C7\text{-}double}$, $(13H)_{C1\text{-}to\text{-}C13\text{-}double}$, and $(14H)_{C1\text{-}to\text{-}C14\text{-}double}$ configurations (Fig. 6(d), (f) and (h), respectively). Concurrently, the red regions between carbon atoms diminish significantly, indicating weaker σ-bonding. However, the elevated electron density on both carbon and hydrogen atoms confirms the formation of stronger π-bonds.

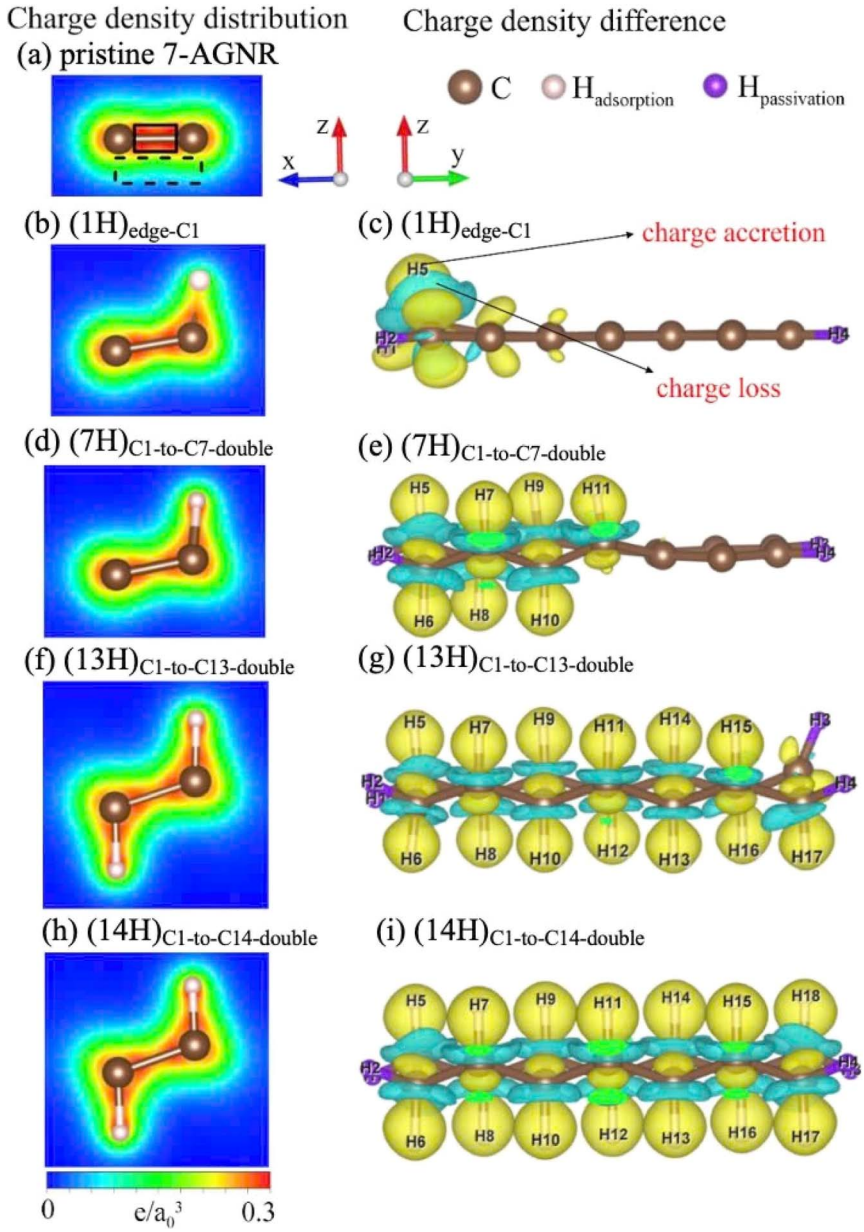

Fig. 6 Charge density distribution of (a) pristine 7-AGNR, (b) $(1H)_{edge\text{-}C1}$, (d) $(7H)_{C1\text{-}to\text{-}C7\text{-}double}$, (f) $(13H)_{C1\text{-}to\text{-}C13\text{-}double}$, (h) $(14H)_{C1\text{-}to\text{-}C14\text{-}double}$ configurations; charge density difference of (c) $(1H)_{edge\text{-}C1}$, (e) $(7H)_{C1\text{-}to\text{-}C7\text{-}double}$, (g) $(13H)_{C1\text{-}to\text{-}C13\text{-}double}$, and (i) $(14H)_{C1\text{-}to\text{-}C14\text{-}double}$ configurations.

These observations are further supported by the charge density difference plots in Fig. 6(e), (g) and (i) for the $(7H)_{C1\text{-}to\text{-}C7\text{-}double}$, $(13H)_{C1\text{-}to\text{-}C13\text{-}double}$, and $(14H)_{C1\text{-}to\text{-}C14\text{-}double}$ configurations, respectively. In these configurations, yellow spheres become more prominent, highlighting the enhanced overlap of H-1s and π-orbitals. Meanwhile, the σ-orbitals transition from large yellow lobes into smaller, more localized yellow spheres near the carbon atoms. This aligns well with the DOS results shown in Fig. 5, where the hybridization of the H-1s and C-$2p_{xy}$ orbitals shifts to lower energy levels as the number of hydrogen atoms increases.

As discussed in previous sections, adsorption of an odd number of H atoms causes orbital intensity and distribution changes, leading to structural and electronic modifications. Fig. 6(a) depicts the charge density distribution of the pristine 7-AGNR, in which the electron clouds (in red) are evenly concentrated on the sp^2 carbon bonds, indicating a stable delocalized π-electron system along the nanoribbon. This structure contrasts with the hydrogenated cases, where distinct regions of charge accumulation and depletion appear. In each of the Fig. 6(c), (e) and (g), there is one unpaired sp^3 hybridized orbital because the number of H atoms in the $(1H)_{edge\text{-}C1}$, $(7H)_{C1\text{-}to\text{-}C7\text{-}double}$, and $(13H)_{C1\text{-}to\text{-}C13\text{-}double}$ configurations are odd. This unpaired sp^3 orbital is expected to cause magnetic moments in the odd-hydrogenated 7-AGNR systems. To gain better insight into this characteristic, the spin density

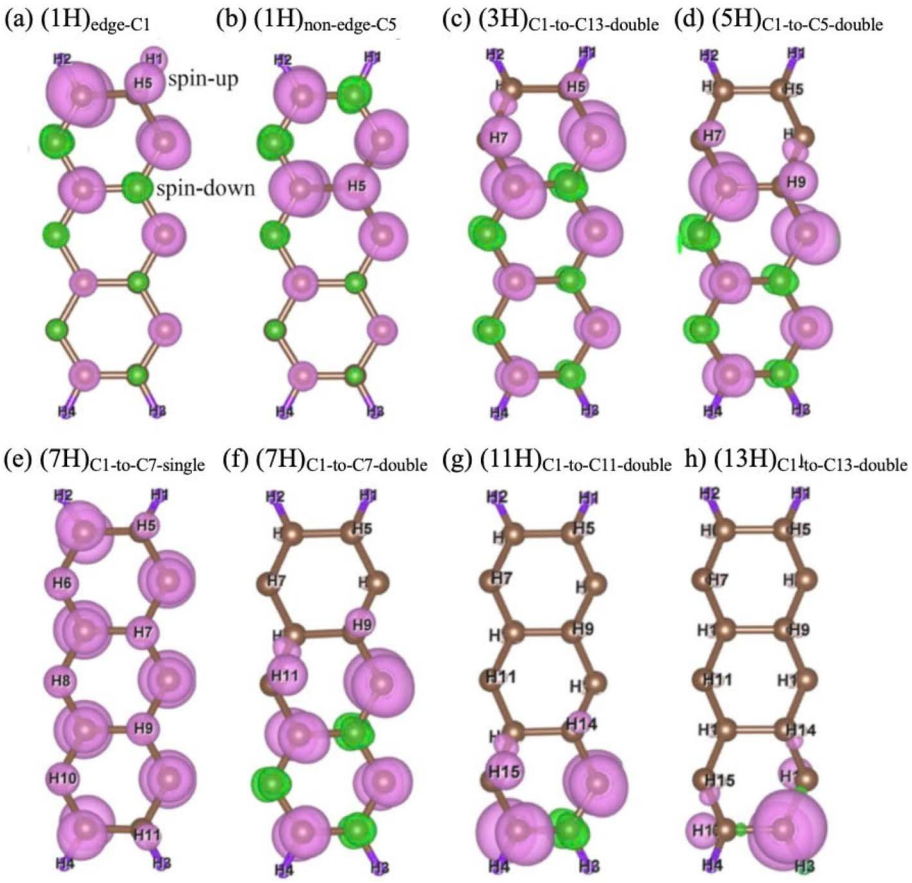

Fig. 7 Spin density distribution of (a) $(1H)_{edge\text{-}C1}$, (b) $(1H)_{non\text{-}edge\text{-}C5}$, (c) $(3H)_{C1\text{-}to\text{-}C13\text{-}double}$, (d) $(5H)_{C1\text{-}to\text{-}C5\text{-}double}$, (e) $(7H)_{C1\text{-}to\text{-}C7\text{-}single}$, (f) $(7H)_{C1\text{-}to\text{-}C7\text{-}double}$, (g) $(11H)_{C1\text{-}to\text{-}C11\text{-}double}$, and (h) $(13H)_{C1\text{-}to\text{-}C13\text{-}double}$ configurations. The magenta and green balls show for the spin-up and spin-down orientations, respectively.

distributions of all odd-hydrogenated 7-AGNRs are calculated and presented in Fig. 7. Magenta and green balls represent spin-up and spin-down orientations, respectively. As shown in Fig. 5, the H-1s orbitals can hybridize with both spin-up and spin-down orbitals of the carbon atoms, leading to significant changes in the spin density of the C atoms. Furthermore, Fig. 6 illustrates that the H-1s orbitals can also influence the spatial arrangement of the C orbitals. These interactions enable hydrogen atoms to modify the spin distribution in 7-AGNRs. The spin density distribution plots for the $(1H)_{edge\text{-}C1}$ and $(1H)_{non\text{-}edge\text{-}C5}$ configurations, shown in Fig. 7(a) and (b), respectively, highlight the impact of the adsorbed H5 adatom. This adatom induces notable distortions in the spin density distribution, affecting both edge and non-edge regions. Specifically, it alters the spin density at edge positions while eliminating spin polarization at non-edge positions. As a result, the overall spin densities in both $(1H)_{edge\text{-}C1}$ and $(1H)_{non\text{-}edge\text{-}C5}$ configurations are non-zero, which induces a magnetic moment. The spin density distributions for the $(3H)_{C1\text{-}to\text{-}C3\text{-}double}$, $(5H)_{C1\text{-}to\text{-}C5\text{-}double}$, $(7H)_{C1\text{-}to\text{-}C7\text{-}double}$, $(11H)_{C1\text{-}to\text{-}C11\text{-}double}$, and $(13H)_{C1\text{-}to\text{-}C13\text{-}double}$ configurations are presented in Fig. 7(c), (d), (f), (g) and (h), respectively. In these cases, the adsorbed hydrogen atoms similarly affect the spin density distribution. However, this effect is limited by the pairing of hydrogen atoms, as the spin contributions of paired hydrogen atoms effectively cancel each other. Consequently, the resulting magnetic moment for these configurations remains constant at 1 μ_B, as reported in Table 2, regardless of the number of hydrogen atoms adsorbed. Due to the adsorption of all H atoms on one side of the 7-AGNR, the difference in spin polarization in $(7H)_{C1\text{-}to\text{-}C7\text{-}single}$ is not limited by the pairing of hydrogen atoms. Fig. 7(e) shows that the nanoribbon is filled with spin-up on one side. Such strong asymmetry in spin orientation results large magnetic moment of the $(7H)_{single\text{-}side}$ configuration, which is 7 μ_B as reported in Table 2.

4. Concluding remarks

Using DFT calculations, we demonstrate the impact of various hydrogen adsorptions on the 7-AGNR system, shedding light on the underlying adsorption mechanisms. Specifically, we construct various hydrogenated 7-AGNR configurations, incorporating both even-numbered (2, 4, 6, 8, 10, 12, and 14) and odd-numbered (1, 3, 5, 7, 9, 11, and 13) hydrogen adatoms. Our evaluation encompasses their structural, electronic, and magnetic properties. The results indicate that hydrogenation with an even number of hydrogen atoms yields non-magnetic

semiconductors while introducing an odd number of hydrogen adatoms results in ferromagnetic semiconductors. The bandgaps of hydrogenated 7-AGNR systems may either increase or decrease as the number of hydrogen adatoms rises. This observation challenges the prevailing understanding that hydrogen adsorption invariably enlarges the bandgap by disrupting the delocalized π-orbitals within the 7-AGNRs. To further elucidate these discrepancies, we conduct an in-depth analysis of the orbital-projected 1D electronic band structures, atom-decomposed electronic band structures, spin-splitting electronic band structures, as well as the orbital- and spin-decomposed DOSs. Additionally, we explore charge density distribution, charge density differences, and spin density distributions. Our analysis reveals significant interactions between the H-1s orbitals and C-2p_z orbitals across a broad energy range, while H-1s orbitals also interact with C-2p_{xy} orbitals in lower valence bands. This dual interaction leads to two notable effects: the formation of sp^3 hybridization, which induces local buckling in the hydrogenated 7-AGNRs, and the development of strongly localized orbitals that diminish the delocalized π-orbitals, ultimately resulting in a reduction of the band gap. As the quantity of hydrogen atoms increases, the interaction between H-1s and C-2p_z orbitals in higher valence bands prevails, thereby enhancing delocalized π-orbitals and expanding the band gap. Interestingly, in cases where hydrogenation occurs with an even number of hydrogen adatoms, we observe a potential reduction in the band gap, as paired hydrogen adatoms on the same plane can counterbalance one another's effects. In contrast, the adsorption of an odd number of hydrogen adatoms consistently increases the band gap, with this effect becoming more pronounced with the addition of hydrogen adatoms due to the asymmetric distribution on one side of the nanoribbon. Regarding magnetic properties, the hydrogen adatom interacts with the C-2p_z and C-2p_{xy} orbitals, influencing the density of spin-up and spin-down orbitals and affecting the shape and orientation of the carbon orbitals. Consequently, an odd number of hydrogen adatoms generates distinct magnetic moments. When hydrogen adatoms are uniformly distributed on both sides of the 7-AGNRs, the resulting paired atoms exhibit a consistent magnetic moment of 1 μ_B, irrespective of the total number of hydrogen adatoms; this equals the number of hydrogen adatoms present on a single side; notably, the $(7H)_{C1\text{-}to\text{-}C7\text{-}single}$ configuration prevents spin cancellation and yields a net magnetic moment of 7 μ_B, whereas symmetric double-side adsorption produces only 1 μ_B due to the pairing effect. Our theoretical results contribute to a comprehensive understanding of the enriched fundamental properties of hydrogen-adsorbed 7-AGNR systems. The enhanced electronic and magnetic characteristics of these varied hydrogen-adsorbed 7-AGNR systems hold considerable promise for applications in advanced electronics, optoelectronics, and spintronics.

Data availability

The data that supports the findings of this study are available within the article.

Author contributions

D. M. Hoat: conceptualization, investigation, data curation, methodology, formal analysis, visualization, writing – original draft. Vo Khuong Dien: investigation, data curation, visualization, writing – review and editing. Ngoc Thanh Thuy Tran: investigation, visualization, formal analysis, writing – review and editing. Quoc Duy Ho: investigation, visualization, formal analysis, writing – review and editing. Minh Triet Dang: investigation, visualization, formal analysis, writing – review and editing. Huynh Anh Huy: investigation, visualization, formal analysis, writing – review and editing. Duong Trong Nhan: supervision, investigation, data curation, visualization, formal analysis, writing – review and editing. Duy Khanh Nguyen: investigation, visualization, formal analysis, validation, writing – review and editing.

Conflicts of interest

The authors declare that they have no known competing financial interests or personal relationships that could have appeared to influence the work reported in this paper.

Acknowledgements

Duong Trong Nhan and Duy Khanh Nguyen acknowledge the support of Van Lang University (VLU), Ho Chi Minh City, Vietnam.

References

1 V. Khuong Dien, *et al.*, *Phys. Rev. B*, 2023, **108**, 205406.
2 D. K. Nguyen, N. T. Tien, J. Guerrero-Sanchez and D. M. Hoat, *Phys. Chem. Chem. Phys.*, 2024, **26**, 18426–18434.
3 D. K. Nguyen, J. Guerrero-Sanchez and D. M. Hoat, *Phys. E*, 2024, **162**, 116003.
4 V. K. Dien, N. T. Tien, N. D. Khanh, N. T. N. Han and M. F. Lin, *Phys. Rev. B*, 2023, **108**, 205150.
5 T. M. D. Huynh, D. K. Nguyen, T. D. H. Nguyen, V. K. Dien, H. D. Pham and M. F. Lin, *Front. Mater.*, 2021, **7**, 569756.
6 D. K. Nguyen, C. V. Ha, L. T. Hong Gam, J. Guerrero-Sanchez and D. M. Hoat, *RSC Adv.*, 2023, **13**, 33634–33643.
7 D. K. Nguyen, D. Q. Hoang and D. M. Hoat, *RSC Adv.*, 2022, **12**, 9828–9835.
8 D. K. Nguyen, N. T. T. Tran, T. T. Nguyen and M. F. Lin, *Sci. Rep.*, 2018, **8**, 1–12.
9 D. M. Hoat, V. K. Dien, Q. D. Ho, D. P. Dam, N. T. Tien and D. K. Nguyen, *Phys. Chem. Chem. Phys.*, 2024, **26**, 15939–15956.
10 N. T. Tien, N. H. Dang, P. T. Bich Thao, K. D. Vo, D. M. Hoat and D. K. Nguyen, *RSC Adv.*, 2024, **14**, 16445–16458.
11 D. K. Nguyen, Y. T. Lin, S. Y. Lin, Y. H. Chiu, N. T. T. Tran and M. Fa-Lin, *Phys. Chem. Chem. Phys.*, 2017, **19**, 20667–20676.
12 N. H. Dang, *et al.*, *J. Magn. Magn. Mater.*, 2024, **607**, 172394.
13 D. M. Hoat, *et al.*, *Phys. E*, 2025, **172**, 116284.

14 D. P. Dam, *et al.*, *Ceram. Int.*, 2025, DOI: 10.1016/j.ceramint.2025.07.042.
15 T. Y. Mi, N. D. Khanh, R. Ahuja and N. T. Tien, *Mater. Today Commun.*, 2021, **26**, 102047.
16 N. T. Tien, N. Van Ut, B. T. Hoc, T. T. Ngoc Thao and N. D. Khanh, *Adv. Condens. Matter Phys.*, 2019, **2019**, 4715953.
17 S. Lou, B. Lyu, X. Zhou, P. Shen, J. Chen and Z. Shi, *Quantum Front.*, 2024, **3**, 1–12.
18 H. Wang, *et al.*, *Nat. Rev. Phys.*, 2021, **3**, 791–802.
19 *Graphene Science Handbook: Fabrication Methods*, ed. M. Aliofkhazraei, CRC Press, 2016.
20 A. Koutsioukis, K. Spyrou, N. Chalmpes, D. Gournis and V. Georgakilas, *Nanomaterials*, 2022, **12**, 447.
21 X. Zhou and G. Yu, *Adv. Mater.*, 2020, **32**, 1905957.
22 R. M. Jacobberger, *et al.*, *Nat. Commun.*, 2015, **6**, 1–8.
23 J. Cai, *et al.*, *Nature*, 2010, **466**, 470–473.
24 M. Pizzochero and E. Kaxiras, *J. Phys. Chem. Lett.*, 2021, **12**, 1214–1219.
25 A. R. Carvalho, J. H. Warnes and C. H. Lewenkopf, *Phys. Rev. B: Condens. Matter Mater. Phys.*, 2014, **89**, 245444.
26 Q. Q. Dai, Y. F. Zhu and Q. Jiang, *Phys. Chem. Chem. Phys.*, 2014, **16**, 10607–10613.
27 K. Sawada, F. Ishii and M. Saito, *J. Phys. Soc. Jpn.*, 2011, **80**, 044712.
28 N. Kharche, Y. Zhou, K. P. O'Brien, S. Kar and S. K. Nayak, *ACS Nano*, 2011, **5**, 6096–6101.
29 N. Liu, *et al.*, *J. Phys. D: Appl. Phys.*, 2013, **46**, 235101.
30 Y. Y. Sung, H. Vejayan, C. J. Baddeley, N. V. Richardson, F. Grillo and R. Schaub, *ACS Nano*, 2022, **16**, 10281–10291.
31 G. Kresse and J. Hafner, *Phys. Rev. B: Condens. Matter Mater. Phys.*, 1993, **47**, 558.
32 G. Kresse and J. Furthmüller, *Comput. Mater. Sci.*, 1996, **6**, 15–50.
33 D. K. Nguyen, *et al.*, *Mater. Chem. Phys.*, 2025, **343**, 130962.
34 Q. D. Ho, *et al.*, *RSC Adv.*, 2025, **15**, 5889–5894.
35 Q. D. Ho and E. Rauls, *Mater. Today Commun.*, 2023, **36**, 106875.
36 Q. Duy Ho and M. Castillo, *Comput. Mater. Sci.*, 2023, **216**, 111827.
37 Q. D. Ho and E. Rauls, *ChemistrySelect*, 2023, **8**, e202302266.
38 J. P. Perdew, K. Burke and M. Ernzerhof, *Phys. Rev. Lett.*, 1996, **77**, 3865.
39 J. P. Perdew, *et al.*, *Phys. Rev. B: Condens. Matter Mater. Phys.*, 1992, **46**, 6671.
40 H. J. Monkhorst and J. D. Pack, *Phys. Rev. B: Condens. Matter Mater. Phys.*, 1976, **13**, 5188.
41 Y.-E. Yang, Y. Xiao, X.-H. Yan and C.-J. Dai, *Chin. Phys. B*, 2015, **24**, 117204.
42 C. Uthaisar and V. Barone, *Nano Lett.*, 2010, **10**, 2838–2842.
43 D. Krepel and O. Hod, *J. Phys. Chem. C*, 2013, **117**, 19477–19488.
44 N. T. T. Tran, D. K. Nguyen, S. Y. Lin, G. Gumbs and M. F. Lin, *ChemPhysChem*, 2019, **20**, 2473–2481.
45 N. T. T. Tran, G. Gumbs, D. K. Nguyen and M. F. Lin, *ACS Omega*, 2020, **5**, 13760–13769.
46 N. T. T. Tran, D. K. Nguyen, O. E. Glukhova and M. F. Lin, *Sci. Rep.*, 2017, **7**, 1–13.
47 Y. Murata, A. Calzolari and S. Heun, *J. Phys. Chem. C*, 2018, **122**, 11591–11597.
48 Y. Y. Sung, *et al.*, *ACS Nano*, 2022, **16**, 10281–10291.
49 V. Van On, H. Thi Phuong Thuy, H. Van Ngoc, N. T. Tung and D. K. Nguyen, *Mater. Today Commun.*, 2022, **33**, 104193.
50 T. T. Nguyen, V. N. Hoang, T. P. T. Huynh, D. K. Nguyen and V. O. Vo, *Phys. E*, 2022, **142**, 115309.
51 D. Fan, *et al.*, *Int. J. Hydrogen Energy*, 2025, **107**, 452–459.
52 D. Fan, *et al.*, *Int. J. Hydrogen Energy*, 2025, **112**, 493–502.
53 D. Fan, *et al.*, *Int. J. Hydrogen Energy*, 2024, **60**, 342–353.
54 M. Yin, *et al.*, *Chin. J. Phys.*, 2025, **93**, 202–220.